# THE LEADING EDGE VORTEX IN FLEXIBLE WING PROPULSION

**Ravi C. Mysa**[1] **and Kartik Venkatraman**[1]

[1]Department of Aerospace Engineering
Indian Institute of Science
Bangalore, India 560012
kartik@aero.iisc.ernet.in

**Abstract:** The elasto-dynamics coupled with the flow dynamics of the flapping flexible wing affects the propulsive performance. The formation, growth, and transport of the leading edge vortex plays a major role in the low frequency regime of oscillation of the flapping wing. This in turn influences the differential pressure distribution along the flexible foil. The spatial and temporal kinematics of the foil is dependent on this differential pressure distribution. And the spatial phase relation between the differential pressure distribution, foil kinematics, and base input excitation determine the propulsive performance of the oscillating flexible foil. We perform both potential and viscous flow numerical experiments to examine this coupling between the vorticity and the elastodynamics of the oscillating flexible foil to illustrate the mechanisms that are responsible for generating thrust.

## 1 INTRODUCTION

The leading and trailing edge vortex formation, transport, and their interaction, together with the elastodynamics of an oscillating flexible foil is likely to influence propulsive thrust and propulsive efficiency. Here, in this paper, we compare results from potential and viscous incompressible flow theory to establish the conditions under which the influence of flow separation at the leading edge leads to

Propulsion by flapping or heaving a flexible plate or foil in a fluid generates thrust and propels animals either in air or water. The role of vorticity or circulation coupled with the elastodynamics is well understood beginning with [1]'s work that gives insight into the shape of the flexible airfoil from which maximum propulsive performance can be achieved. [2] performed numerical experiments for the large amplitude flexible foil without considering the inertia terms. [3] modeled the flexibility of the structure using springs attached to the membrane body of the airfoil. Oscillating flexible foils produce large thrust at discrete frequencies. [4] showed that at discrete frequencies of heaving in a flexible foil, the thrust coefficient is maximum. Recently, [5], presented results for heaving flexible flat plate in a fluid at Reynolds numbers in the range $7800$ to $46000$. They observe thrust peaks that coincide with frequencies where the trailing edge amplitude is maximum.

In the context of a flexible wing propulsion, the question that naturally arises is if viscous effects are significant. As in the case of potential flow simulations we correlate the fluid dynamics through leading and trailing edge vortex formation and transport, and pressure and thrust, with

elasto-dynamic parameters such curvature, slope and foil accelerations. We study the leading vortex separation and subsequent interaction with flexible foil boundary. Further we investigate the association of the leading edge vortex with the trailing edge vortex for each oscillation cycle.

In the case of a rigid foil, oscillating in heave and pitch, one has a much better appreciation of the fluid dynamics especially the creation and transport of vorticity and its influence on the pressure developed over the airfoil. [6] has shown that optimum maximum angle of attack for larger thrusts is between $56° - 60°$. At these angles of attack the leading edge vortex is in contact with the surface of the airfoil which is the source of large suction force resulting in thrust. The amplitude and frequency dependence on the formation, growth, and transport of the leading edge vortex as well as the nature of the vortex wake has been catalogued by [7].

However elastic flexibility and inertia bring in infinite degrees of freedom that change the shape of the foil during deflection, and that in turn drastically influence the fluid dynamics over the foil. In contrast, in the case of a rigid foil, the leading edge suction force is the only force acting in the thrust direction. In a heaving flexible foil, apart from the leading edge suction force, circulatory and non-circulatory pressure forces, together with the time and spatially varying shape of the foil play a significant role in determining the thrust.

## 2 THE FLUID-ELASTIC MODEL

The equation of motion of the foil is in terms of the vibration of a cantilevered Euler-Bernoulli beam and distributed fluid dynamic forces on it. Since the fluid dynamics is two-dimensional, we consider unit span of the foil or beam. The governing equation is

$$m\frac{\partial^2 h(x,t)}{\partial t^2} + c\frac{\partial^5 h(x,t)}{\partial t \partial x^4} + EI\frac{\partial^4 h(x,t)}{\partial x^4} = \Delta p(x,t)\hat{\boldsymbol{n}} \cdot \hat{\boldsymbol{k}} - m\frac{d^2 h_b(t)}{dt^2}; \quad 0 < x < L. \quad (1)$$

The pressure across the foil surface can be shown to be

$$\Delta p(x,t) \triangleq p^- - p^+ = \rho_\infty U_\infty \gamma(x,t) + \rho_\infty \frac{\partial}{\partial t}\int_0^x \gamma(\xi,t)d\xi. \quad (2)$$

The no-normal flow boundary condition on the foil surface gives us

$$U_\infty \frac{\partial h(x,t)}{\partial x} + \frac{dh_b(t)}{dt} + \frac{\partial h(x,t)}{\partial t} = \\ -\frac{1}{2\pi}\int_0^L \frac{\gamma(\xi,t)\big(x-\xi\big)}{\big(x-\xi\big)^2 + \big(h(x,t) - h(\xi,t)\big)^2}d\xi + \\ -\frac{1}{2\pi}\sum_{i=1}^{N_w} \frac{\Gamma_i^w\big(x-\tilde{x}_i\big)}{\big(x-\tilde{x}_i\big)^2 + \big(h(x,t) - \tilde{z}_i\big)^2}. \quad (3)$$

The vorticity distribution $\gamma(x,t)$ is determined by solving the above integro-differential equation. In order to do so, we need to invoke the Kutta condition to uniquely determine the circulation around the foil. The Kutta condition for steady and unsteady flow states that the fluid

velocity leaves the trailing edge of the foil smoothly. For steady flow this translates to the condition $\gamma(L) = 0$. For unsteady flow this condition is realized by asserting that the pressure across the wake surface is zero or the wake is a mass-less membrane and cannot support an acceleration.

Solving the above coupled equations, one could determine the displacement response of the flexible foil as well as the pressure difference across it. Closed form solutions are possible with simplifying assumptions. However we chose a numerical approximation to arrive at the solution.

The coupled fluid elastic equations are solved using a finite element discretization for the Euler-Bernoulli beam and a discrete vortex panel discretization of the vorticity equation. The number of finite elements for modelling the flexible foil elasto-dynamics was chosen to be equal to the number of discrete vortex panels — 30 in number. This was chosen on the basis of convergence studies on free-vibration as well as fluid dynamic tests on some text-book examples. For the elasto-dynamics of the foil, the number of elements are considered such that first ten natural modes of the cantilevered beam are accurately captured and included in the response. Convergence test was done unto the tenth mode by varying the number of finite elements. The coupled problem of fluid-elasticity is numerically using a predictor-corrector type algorithm.

In order to investigate the influence of viscosity on propulsive performance of the oscillating flexible foil, we coupled the foil dynamics with an incompressible Navier-Stokes flow solver. The Euler-Bernoulli beam equation is then

$$m\frac{\partial^2 h(x,t)}{\partial t^2} + c\frac{\partial^5 h(x,t)}{\partial t \partial x^4} + EI_{yy}\frac{\partial^4 h(x,t)}{\partial x^4} = \Delta p(x,t)\hat{\boldsymbol{n}} \cdot \hat{\boldsymbol{k}} - m\frac{d^2 h_b(t)}{dt^2}; \quad 0 < x < L. \quad (4)$$

The governing equations of the incompressible viscous flow are the Navier-Stokes equations with a constant viscosity term. The boundary conditions near the immersed boundary are applied using the sharp interface procedure [8]. The discretized momentum equation is solved using the Gauss-Sidel point by point iteration. The pressure Poisson equation is solved using a preconditioned Bi-CGSTAB, a Krylov subspace based method. Stone's implicit pre-conditioner [9] is used for the Poisson equation solver. As the convection term is treated explicitly, the time marching problem is restricted by the CFL number criteria.

$$\frac{\partial u_i}{\partial x_i} = 0,$$

$$\frac{\partial u_i}{\partial t} + \frac{\partial u_i u_j}{\partial x_j} = -\frac{1}{\rho}\frac{\partial p}{\partial x_i} + \nu\frac{\partial}{\partial x_j}\left(\frac{\partial u_i}{\partial x_j}\right). \quad (5)$$

These equations are solved numerically using a cell-centered and collocated arrangement for the component velocities $u_i$ and the pressure $p$ in a non-uniform Cartesian grid defined in a Cartesian space $x_i$ along with temporal variable $t$. The governing equations are solved using the fractional step method of [10]. The first sub-step solves a modified momentum equation numerically for the intermediate velocity $u_i^*$ which is used in evaluating the fluid velocities $u_i^{n+1}$ at time $n+1$. The convective terms are discretized using a second order Adams-Bashforth scheme and the diffusive terms are implicitly discretized using a Crank-Nicolson scheme.

3

(a) thrust coefficient in viscous flow

(b) thrust coefficient in potential flow

(c) propulsive efficiency in viscous flow

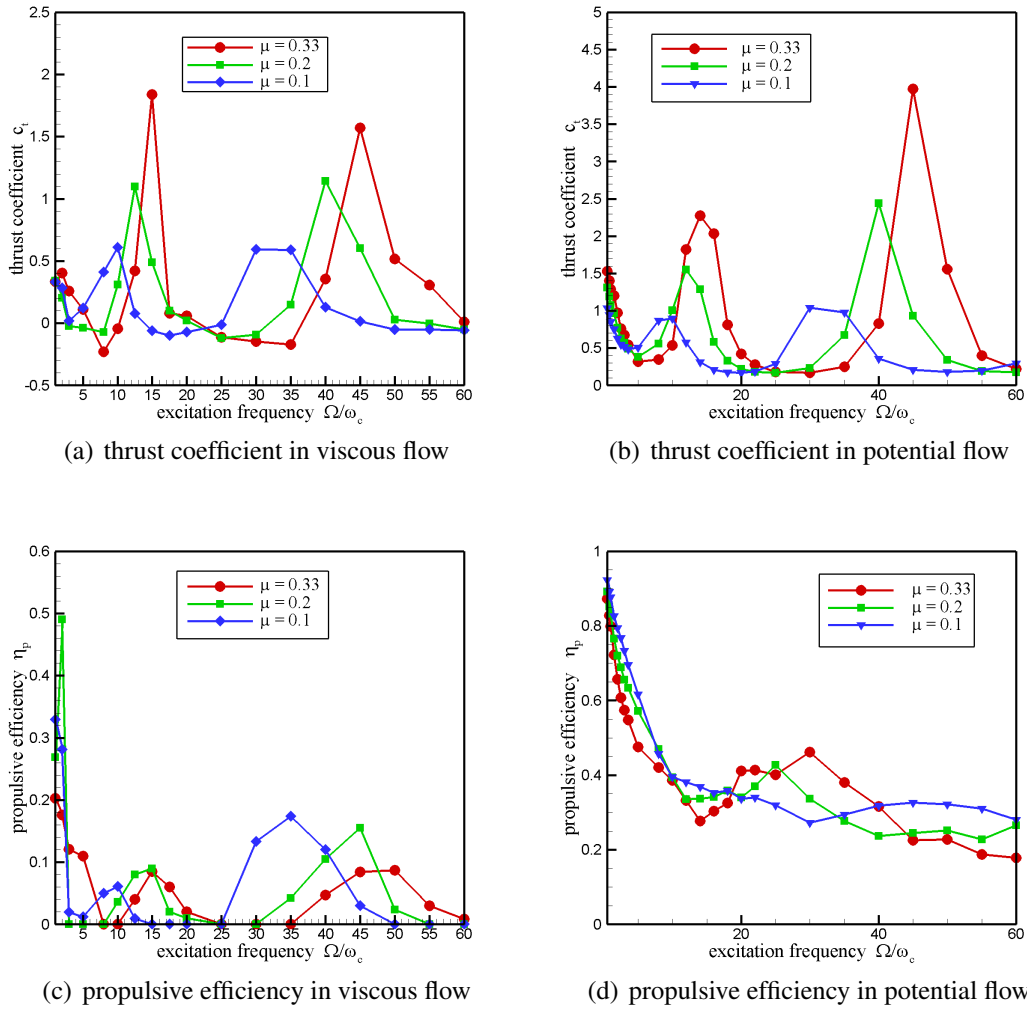(d) propulsive efficiency in potential flow

Figure 1: Thrust coefficient and propulsive efficiency in viscous and potential flow as a function of excitation frequency for different mass ratios

The Dirichlet boundary condition is applied to solve the modified momentum equation and the Neumann boundary condition for the pressure Poisson equation. The grid is finely resolved in the region where the motion of the body occurs. Care is taken that the grid size varies smoothly from finer grid to coarser grid and the variations from fine grid to coarse grid done using an exponential function.

A non-uniform Cartesian grid is developed in which the body with complex boundary of interest is placed. The grid is finely resolved in the region where the motion of the body occurs. Care is taken that the grid size varies smoothly from finer grid to coarser grid and the variations from fine grid to coarse grid done using an exponential function.

## 3 DISCUSSION

### 3.1 Propulsive performance

We compare the propulsive performance using both the potential flow as well as the viscous flow models. In Figure 1 is shown the thrust coefficient and propulsive efficiency obtained using the incompressible Navier-Stokes solver as well as the unsteady potential solver. In the

entire frequency range the numerical values of the propulsive efficiency predicted by the two solvers differs appreciably. Further, the viscous solver predicts drag at some frequencies of oscillation, which the potential flow solver cannot predict. Understandably the coefficient of thrust predicted by the potential flow model is higher than that predicted by the Navier-Stokes solver since viscous drag is not accounted by the potential flow model. Now in the low frequency range approximately between $1 \leq \bar{\Omega} \leq 8$, the qualitative nature of variation with frequency of the coefficient of thrust and propulsive efficiency is different. As we see below, this has to do with the leading edge vortex formation.

The tables below gives the numerical values of the peaks seen in the thrust and propulsive efficiency predicted by both the solvers.

Table 1: Natural frequencies $\bar{\omega}_i$ and resonance frequencies $\bar{\Omega}_i$ for the foil oscillating in a viscous flow

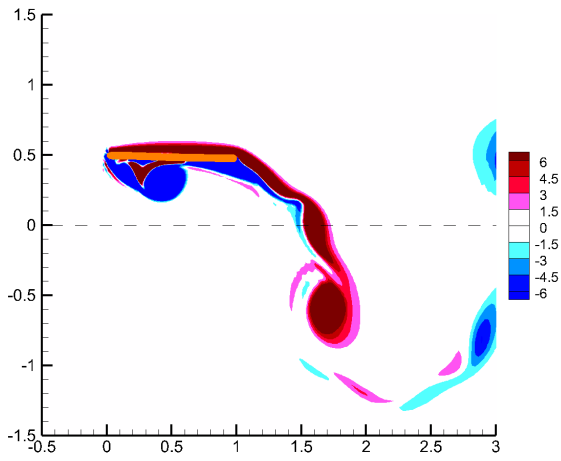| Mass ratio | Natural frequencies in vacuum | Impulse response maxima frequencies | Thrust maxima frequencies |
|---|---|---|---|
| $\mu = 0.33$ | $\bar{\omega}_1 = 3.4$ | $\bar{\Omega}_1 = 1.5$ | $\bar{\Omega}_1 = 2.0$ |
| | $\bar{\omega}_2 = 21.9$ | $\bar{\Omega}_2 = 14.6$ | $\bar{\Omega}_2 = 16.0$ |
| | $\bar{\omega}_3 = 61.7$ | $\bar{\Omega}_3 = 46.0$ | $\bar{\Omega}_3 = 45.0$ |
| $\mu = 0.2$ | $\bar{\omega}_1 = 3.4$ | $\bar{\Omega}_1 = 1.5$ | $\bar{\Omega}_1$ NA |
| | $\bar{\omega}_2 = 21.9$ | $\bar{\Omega}_2 = 12.6$ | $\bar{\Omega}_2 = 13.0$ |
| | $\bar{\omega}_3 = 61.7$ | $\bar{\Omega}_3 = 40.4$ | $\bar{\Omega}_3 = 40.0$ |
| $\mu = 0.1$ | $\bar{\omega}_1 = 3.4$ | $\bar{\Omega}_1 = 0.8$ | $\bar{\Omega}_1$ NA |
| | $\bar{\omega}_2 = 21.9$ | $\bar{\Omega}_2 = 10.0$ | $\bar{\Omega}_2 = 10.5$ |
| | $\bar{\omega}_3 = 61.7$ | $\bar{\Omega}_3 = 32.0$ | $\bar{\Omega}_3 = 30.0$ |

Table 2: Natural frequencies $\bar{\omega}_i$ and resonance frequencies $\bar{\Omega}_i$ for the foil oscillating in a potential flow

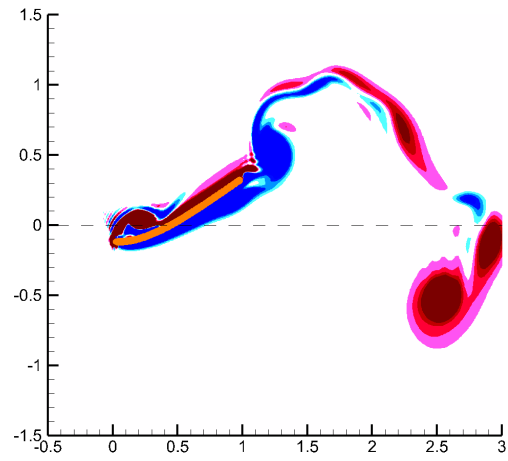| Mass ratio | Natural frequencies in vacuum | Impulse response maxima frequencies | Thrust maxima frequencies |
|---|---|---|---|
| $\mu = 0.33$ | $\bar{\omega}_1 = 3.4$ | $\bar{\Omega}_1 = 3.8$ | $\bar{\Omega}_1 = $ NA |
| | $\bar{\omega}_2 = 21.9$ | $\bar{\Omega}_2 = 15.3$ | $\bar{\Omega}_2 = 14.0$ |
| | $\bar{\omega}_3 = 61.7$ | $\bar{\Omega}_3 = 46.0$ | $\bar{\Omega}_3 = 45.0$ |
| $\mu = 0.2$ | $\bar{\omega}_1 = 3.4$ | $\bar{\Omega}_1 = 3.8$ | $\bar{\Omega}_1$ NA |
| | $\bar{\omega}_2 = 21.9$ | $\bar{\Omega}_2 = 11.5$ | $\bar{\Omega}_2 = 12.0$ |
| | $\bar{\omega}_3 = 61.7$ | $\bar{\Omega}_3 = 42.0$ | $\bar{\Omega}_3 = 40.0$ |
| $\mu = 0.1$ | $\bar{\omega}_1 = 3.4$ | $\bar{\Omega}_1 = $ NA | $\bar{\Omega}_1$ NA |
| | $\bar{\omega}_2 = 21.9$ | $\bar{\Omega}_2 = 11.5$ | $\bar{\Omega}_2 = 10.0$ |
| | $\bar{\omega}_3 = 61.7$ | $\bar{\Omega}_3 = 34.6$ | $\bar{\Omega}_3 = 30.0$ |

## 3.2 Leading edge vortex

We now take a look at the snapshots of the vorticity contours about the flexible foil for one-half cycle of oscillation, both for the viscous flow as well as the potential flow. These snapshots are taken at intervals of $\pi/5$ of phase for the flexible foil plunging from the top during a downstroke. The frequency of oscillation is $\bar{\Omega} = 2$, and as seen in Table 1 above, at this frequency of oscillation the thrust is a maxima.
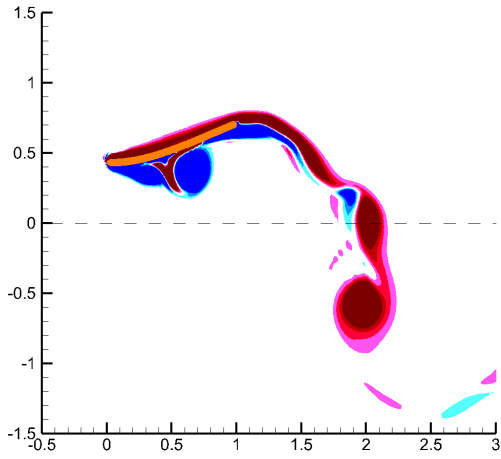
The snapshots for the potential flow simulation at this frequency of oscillation is in start con-
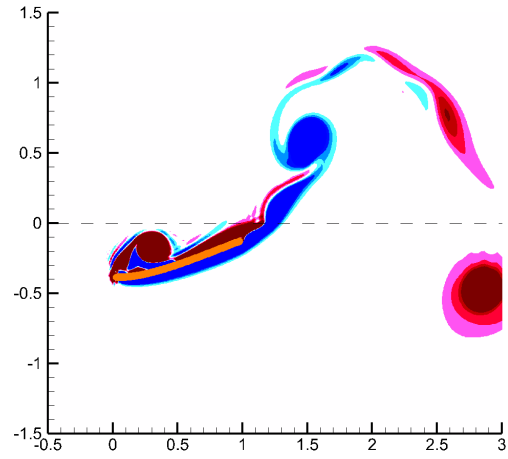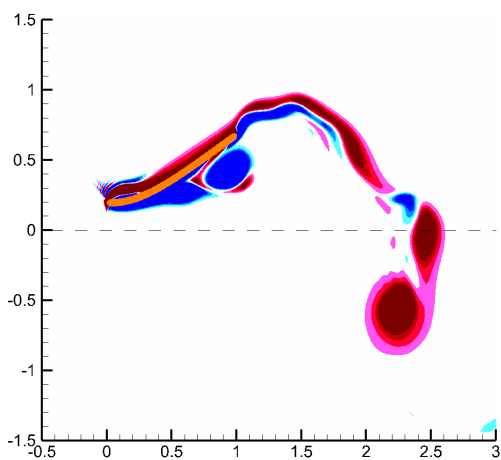
(a) $\bar{\Omega}\tau = \pi/2$
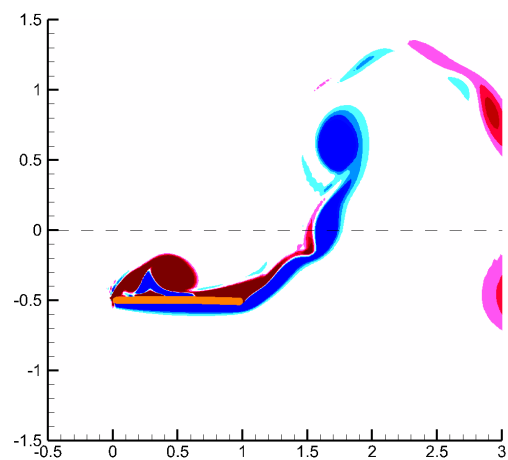
(d) $\bar{\Omega}\tau = \pi/2 + 3\pi/5$

(b) $\bar{\Omega}\tau = \pi/2 + \pi/5$

(e) $\bar{\Omega}\tau = \pi/2 + 4\pi/5$

(c) $\bar{\Omega}\tau = \pi/2 + 2\pi/5$

(f) $\bar{\Omega}\tau = 3\pi/2$

Figure 2: Wake vorticity contours for viscous flow at $\bar{\Omega} = 2.0$ and $\mu = 0.33$

(a) $\bar{\Omega}\tau = \pi/2$

(b) $\bar{\Omega}\tau = \pi/2 + \pi/5$

(c) $\bar{\Omega}\tau = \pi/2 + 2\pi/5$

(d) $\bar{\Omega}\tau = \pi/2 + 3\pi/5$

(e) $\bar{\Omega}\tau = \pi/2 + 4\pi/5$
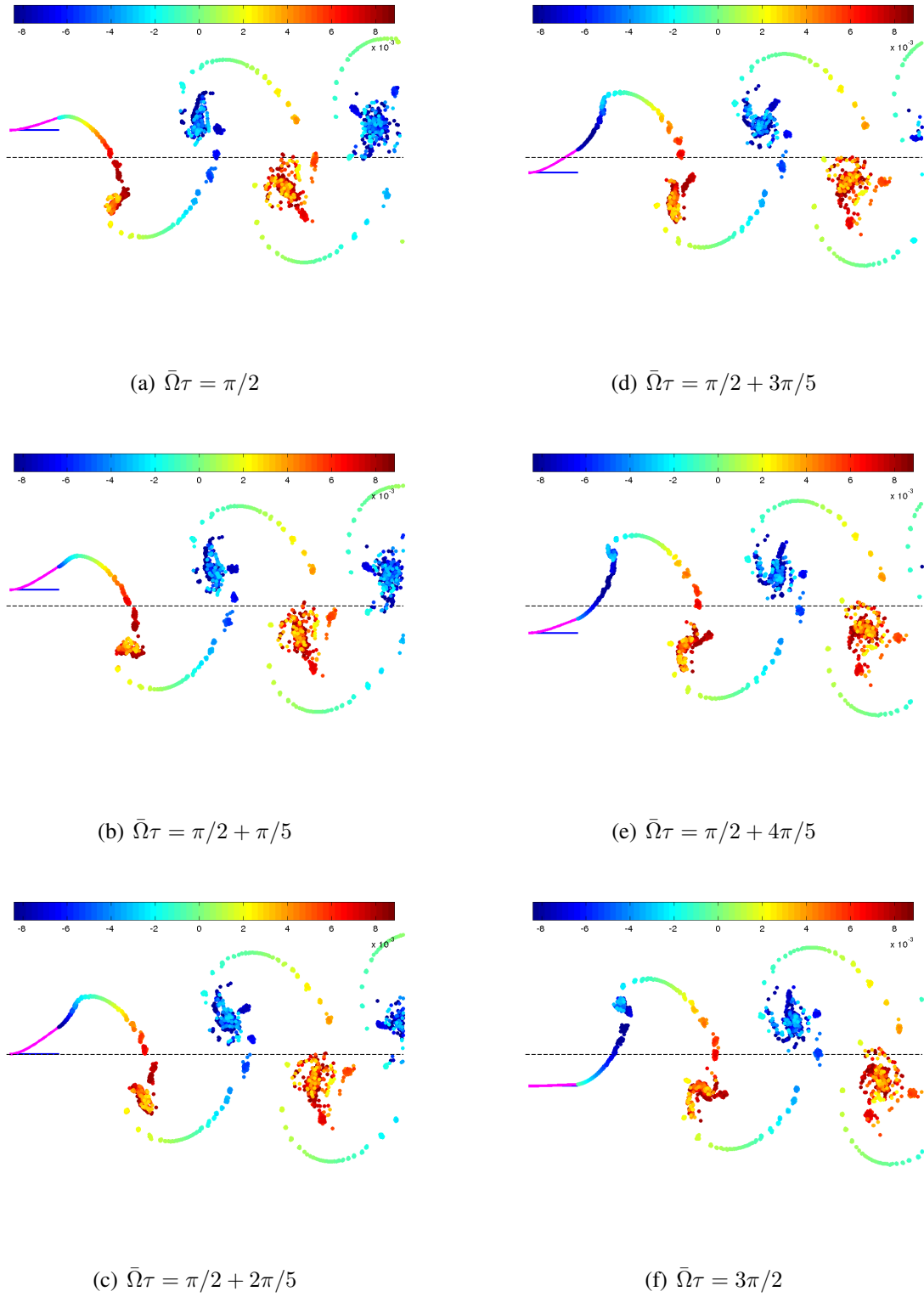
(f) $\bar{\Omega}\tau = 3\pi/2$

Figure 3: Wake vorticity contours for potential flow at $\bar{\Omega} = 2.0$ and $\mu = 0.33$

trast. The leading edge vortex is absent—that is obvious—but the trailing edge vortex is also different. The potential flow simulation sheds a vortex at each time-step in order to satisfy Kelvin's theorem. At the most it can capture the deflection of the wake and the reverse von Kármán wake pattern that is indicative of a thrust producing oscillation. The viscous flow simulation, on the other hand captures the formation of the leading edge vortex, its growth and well as transport over the surface of the airfoil, the influence of the airfoil deflection, slope, and curvture on the growth and transport, and finally the interaction with the leading edge vortex and the wake at the trailing edge.

Figure 4 shows the contours of kinematics of the elastic response of the foil for the excitation frequency 2.0. The x-axis corresponds to one time-period of excitation and the y-axis the length of the foil. In particular note the foil slope and curvature — Figures 4(a) and 4(b), and the differential pressure Figure 4(e). Note that the pressure on the foil is generated in regions where the curvature and slope together are high. Together, the curvature and slope, create an asymmetrical solid boundary relative to the free-stream leading to creation of vorticity. This is the region where the primary leading edge vortex is formed and transported before loosing its strength further aft of the mid-chord, as can be seen in the snapshots in Figure **??**. The pressure contour Figure 4(e) is tilted to the right indicative of a forward moving pressure disturbance due to the movement of the leading edge vortex towards the trailing edge. In the same pressure contour plot, Figure 4(e), there is a region between $0.6 < \bar{x} < 0.8$ along the length of the foil where there are small narrow islands of high pressure differential. These are caused by the transverse and angular accelerations of the foil — Figures 4(c) and 4(d). This pressure peak is non-circulatory in origin.

The rightward tilt of the pressure contour from the leading edge is absent for the potential flow simulation as shown in the Figure 4(f) as now there is no formation and transport of the leading edge vortex.

In Figure 5 the elasto-dynamics of the foil together with the pressure contours are shown. These contour diagrams illustrate the spatial and temporal variation of the variable of interest. The y-axis denotes the length of the foil and the x-axis time corresponding to one time period of the external excitation. First we have presented the slope of the deflection of the flexible foil in Figure 5(a). The slope is zero at the leading edge and increases along the length of the foil to a maximum value at the trailing edge as shown. FIgure **??** should be kept in mind while we discuss these diagrams. The curvature is maximum at the leading edge and minimum at the training edge as shown in the Figure 5(b). The displacement, slope, and curvature define the topology of the deflection of the flapping foil. The circulatory pressure is directly proportional to the bound circulation and the corresponding contour circulatory pressure plot is shown in Figure 5(e). The pressure is high in a region where the curvature is high and also, in a weak sense, in the region where the slope is high. This is understandable as the slope and curvature of the foil cause velocity gradients in the flow and consequently pressure gradients. But this is not complete without including the accelerations of the foil, namely the vertical translational and angular acceleration shown in Figures 5(c) and 5(d) respectively. The non-circulatory pressure is shown in Figure 5(f) and note the regions of high pressure are the regions of high accelerations of the foil [11, chapter 13]. The total pressure reflects the contribution of the circulatory and non-circulatory pressures. Note that the non-circulatory pressure magnitude is significantly less in magnitude relative to the circulatory pressure.

The differential pressure contours from the viscous and potential flow simulations shown in
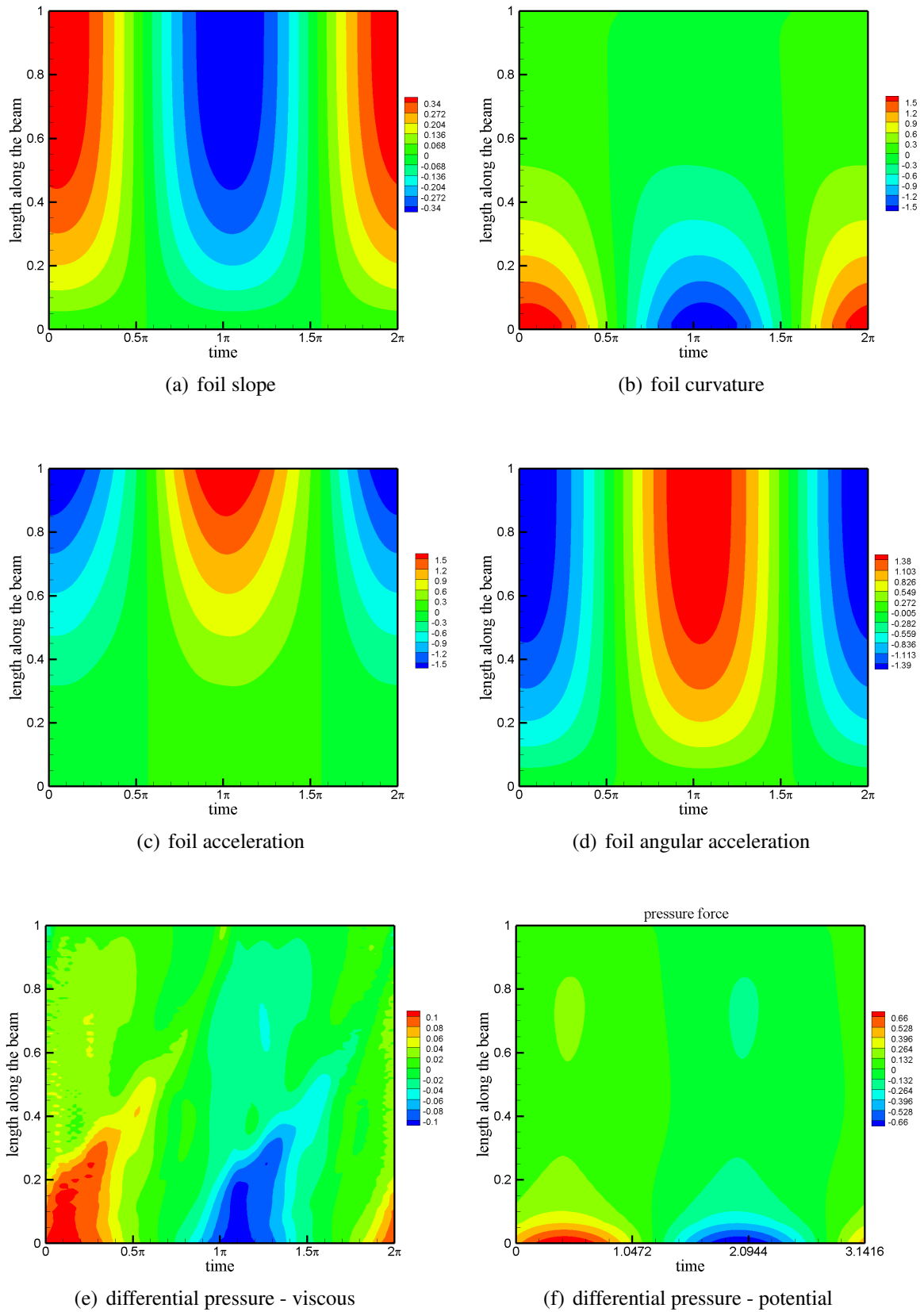
(a) foil slope

(b) foil curvature

(c) foil acceleration

(d) foil angular acceleration

(e) differential pressure - viscous

(f) differential pressure - potential

Figure 4: Contours of elasto-dynamics and pressure for $\bar{\Omega} = 2.0$ from viscous flow simulations

(a) foil slope

(b) foil curvature
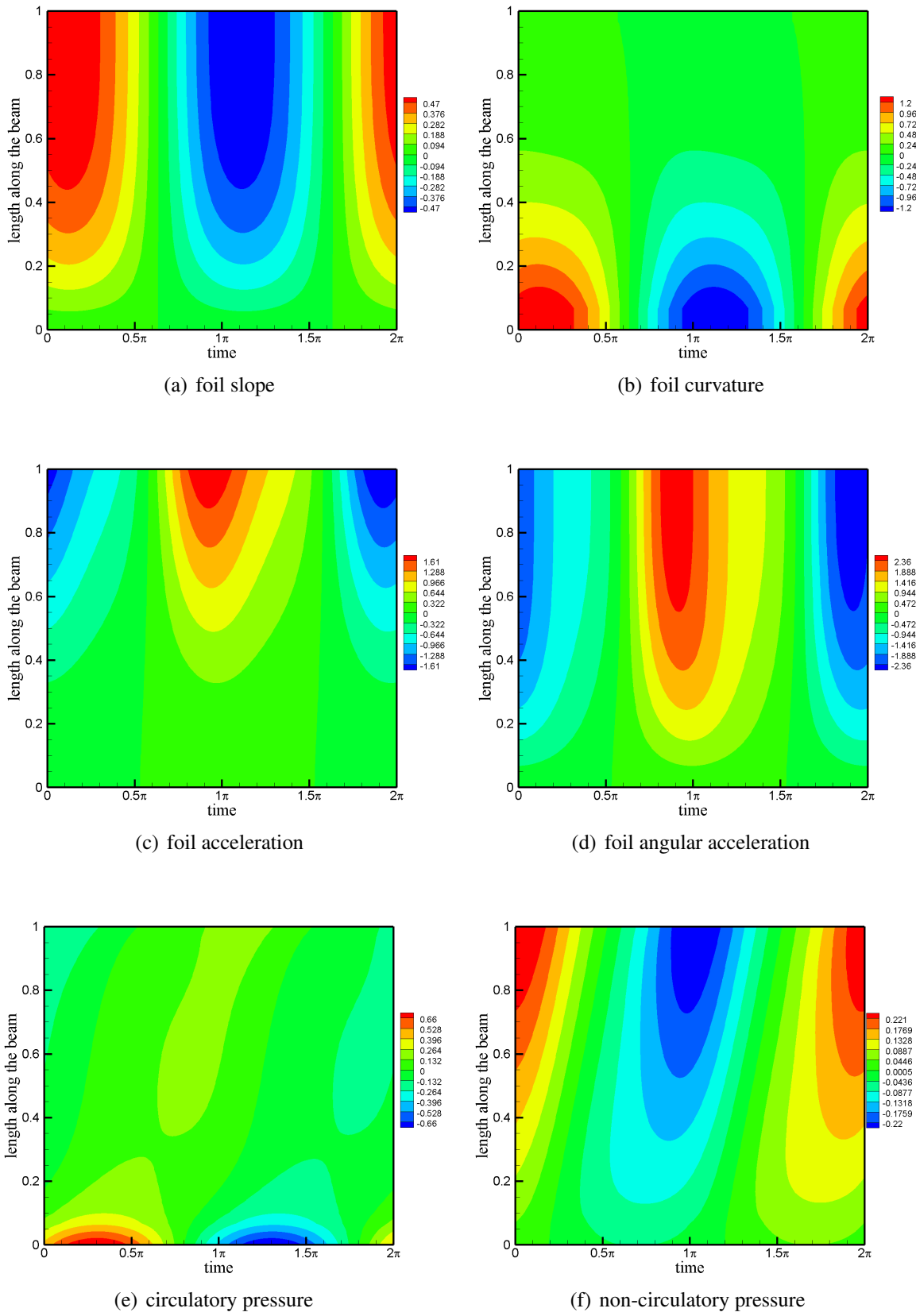
(c) foil acceleration

(d) foil angular acceleration

(e) circulatory pressure

(f) non-circulatory pressure

Figure 5: Contours of elasto-dynamics and pressure for $\bar{\Omega} = 2.0$ from potential flow simulations

(a) pressure force and slope of foil
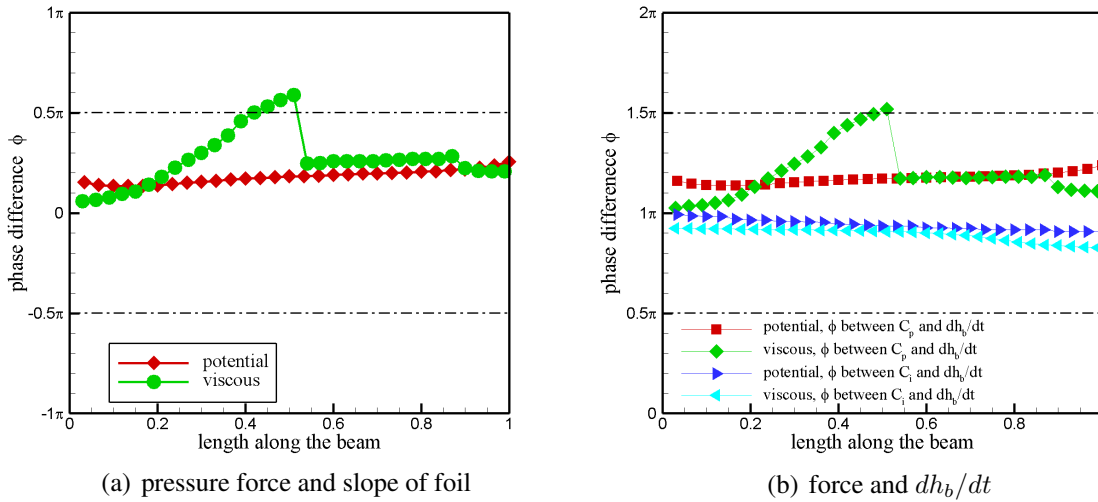
(b) force and $dh_b/dt$

Figure 6: Phase difference between forces on the foil and foil kinematics $\bar{\Omega} = 2.0$ from viscous and potential flow simulations

Figure 4 in fact reveal the extent to which the viscous flow model is different than the potential flow model. And this difference could be attributed to capturing the formation, growth, and transport of the leading edge vortex over the foil surface. This difference in the computed pressure difference in turn affects the foil kinematics as well as its dynamics.

At higher frequencies beyond $\bar{\Omega} > 10$ the leading edge vortex formation is not present at all. This has to do with alternates foil deformation shape especially the changing curvature one encounters in mode shapes at higher frequencies. This causes flow separation and re-attachment over the foil surface and consequently affects the mode pressure loading on the flexible foil.

The variation of the phase difference between pressure force and slope for both viscous and potential flows are shown in the Figure 6(a). For the viscous case, near the leading edge the vortex formed causes forces which are in phase with the slope. Along the length of the beam the leading edge vortex moves and so the phase difference also increases. At mid-length there is a sudden jump in the phase difference because from that point onwards the non-circulatory pressure forces dominate. Apart from pressure due to the leading edge vortex, non-circulatory forces due to the acceleration of the foil also contribute to the thrust. The phase difference for the potential flow is almost constant with a slight increase along the length of the foil.

The phase difference between the pressure force and base excitation velocity is almost $180°$ more than the phase difference between the pressure force and slope as shown in the Figure 6(b). Note that a phase difference between $0 < \phi < \pi/2$ and $3\pi/2 < \phi < 2\pi$ implies positive work done by the force on the system or energy is added, while $\pi/2 < \phi < 3\pi/2$ denotes negative work done by the force on the system or energy is extracted from the system. Here the system refers to the elastic solid with its flexibility and damping. The fluid pressure force does negative work through out the length of the beam. In the first half of the foil length these pressure forces caused by the leading edge vortex. Beyond the mid-point though the pressure forces are caused primarily due to non-circulatory or inertial effects. Therefore the system loses energy to the flow along the length of the foil. The inertia force does negative work on the system or subtracts energy to the system throughout the length of the foil.

11

## 4 CONCLUSIONS

Using two-dimensional incompressible inviscid and viscous flow models coupled to a Bernoulli-Euler model of a one-dimensional elastic solid in flexure, we have shown that the interplay of elasto-dynamics of the flexible foil with the vorticity and inertia in the fluid is primarily responsible for thrust and drag in flapping. In the case of a flapping foil, our interrogation of the vorticity and elastodynamics reveal that pressure on the foil at low oscillation frequencies are circulatory or vortical in nature caused primarily by the leading edge vortices. These leading edge vortices do not separate over the foil aided by favorable pressure gradients induced by the slope and curvature of the foil. At moderate and high frequencies the differential pressure is non-circulatory in origin caused by high flapping frequencies. Thrust peaks at discrete frequencies close to the natural frequencies of vibration of the elastic foil. We have also studied the propulsive efficiency of a flapping foil; at low frequencies it is very high due to low input power as the frequency of oscillation is low, and falls with increase in flapping frequency. The propulsive efficiency too peaks at discrete frequencies that are distinct but close to the frequency peaks for thrust. We have shown that the input power that determines efficiency is determined by the phase relation between the differential pressure and flapping velocity over the foil.

## 5 REFERENCES

[1] Lighthill, M. J. (1960). Note on the swimming of slender fish. *Journal of Fluid Mechanics*, 9(2), 305–317.

[2] Katz, J. and Weihs, D. (1978). Hydrodynamic propulsion by large amplitude oscillation of an airfoil with chordwise flexibility. *Journal of Fluid Mechanics*, 88(03), 485–497.

[3] Pederzani, J. and Haj-Hariri, H. (2006). Numerical analysis of heaving flexible airfoils in a viscous flow. *AIAA Journal*, 44(11), 2773–2779.

[4] Michelin, S. and Smith, S. G. L. (2009). Resonance and propulsion performance of a heaving flexible wing. *Physics of Fluids*, 21(071902), 1–15.

[5] Quinn, D. B., Lauder, G. V., and Smits, A. J. (2014). Scaling the propulsive performance of heaving flexible panels. *Journal of Fluid Mechanics*, 738, 250–267.

[6] Wang, Z. J. (2000). Vortex shedding and frequency selection in flapping flight. *Journal of Fluid Mechanics*, 410, 323–341.

[7] Lewin, G. C. and Haj-Hariri, H. (2003). Modelling thrust generation of a two-dimensional heaving airfoil in a viscous flow. *Journal of Fluid Mechanics*, 492, 339–362.

[8] Mittal, R., Dong, H., Bozkurttas, M., et al. (2008). A versatile sharp interface immersed boundary method for incompressible flows with complex boundaries. *Journal of Computational Physics*, 227, 4825–4852.

[9] Ferziger, J. H. and Peric, M. (2002). *Computational Methods for Fluid Dynamics*. Berlin Heidelberg New York: Springer.

[10] Kan, J. V. (1986). A second-order occurate pressure-correction scheme for viscous incompressible flow. *SIAM Journal of Scientific and Statistical Computing*, 7, 870–891.

[11] Katz, J. and Plotkin, A. (2001). *Low-Speed Aerodynamcis*. Cambridge University Press, 2 ed.

**COPYRIGHT STATEMENT**

The authors confirm that they, and/or their company or organization, hold copyright on all of the original material included in this paper. The authors also confirm that they have obtained permission, from the copyright holder of any third party material included in this paper, to publish it as part of their paper. The authors confirm that they give permission, or have obtained permission from the copyright holder of this paper, for the publication and distribution of this paper as part of the IFASD-2017 proceedings or as individual off-prints from the proceedings.